Geometric Quantum Tunneling in the MMA–DMF Framework

Paulo Adriano
Independent Researcher
Correspondence: home@chiptec.net

Abstract

We present a technical validation of Geometric Quantum Tunneling (GQT) within the MMA-DMF framework. In this approach, barrier penetration is not postulated: it emerges as a deterministic, noise-assisted escape process generated by a scalar-field generalized Langevin dynamics whose stochastic sector is thermodynamically closed by a strict fluctuation–dissipation relation [1, 2] and regulated by a finite ultraviolet (UV) cutoff at a fundamental scale $M \simeq 1.00 \times 10^2$ TeV. We report 1D benchmark results showing (i) Schrödinger-like dispersion calibration at Nelson equilibrium, (ii) WKB recovery via exponential transmission scaling with barrier width (linear $\ln T$ vs width with $R^2 > 0.99$ and a consolidated WKB recovery error of 1.2%), (iii) quantitative isomorphism against transfer-matrix quantum mechanics across energy regimes (deep-tunneling RMSE 0.042, resonant RMSE 0.085, classical-transport RMSE 0.011), and (iv) the distinctive "geometric wall" prediction that tunneling collapses as $V_0/M \to 1$ (rapid suppression already near $V_0 \approx 0.95M$ and an inferred cutoff near $0.98M$ in the consolidated summary). We include mandatory ablations via the geometric toggle β_{geo} (tunneling vanishes as $\beta_{\text{geo}} \to 0$), and stability/convergence constraints requiring $dt \lesssim 0.01\, M^{-1}$ with validated production operation at $dt = 0.005\, M^{-1}$ and an energy drift slope 3.4×10^{-6} over $T_{\max} = 1000$. Finally, we specify a reproducibility and integrity layer (bit-exact seed replay across hardware targets, deterministic checkpointing, and SHA-256 manifesting) intended to make the full pipeline externally auditable. The consolidated evidence supports that MMA-DMF reproduces standard low-energy tunneling phenomenology while making a falsifiable high-energy prediction tied to UV regulation.

Keywords: quantum tunneling; WKB approximation; transfer-matrix method; generalized Langevin equation; fluctuation–dissipation theorem; colored noise; ultraviolet cutoff; interferometry

Contents

1 Introduction

Quantum tunneling is traditionally treated as a foundational feature of nonrelativistic quantum mechanics [3, 4, 5, 6, 7]: a wavefunction penetrates classically forbidden regions with a transmission probability determined by the barrier geometry and particle energy. The MMA-DMF framework adopts a different stance. It models tunneling as an emergent statistical outcome of deterministic scalar-field dynamics coupled to a structured vacuum sector represented by colored stochastic forcing, with the forcing amplitude thermodynamically locked to dissipation by a strict fluctuation–dissipation closure [1, 2]. A finite ultraviolet (UV) cutoff at scale M regulates the vacuum spectrum and introduces a qualitatively new prediction at high barrier heights.

This paper has two aims. First, in the regime where standard quantum mechanics is well tested, the framework must reproduce semiclassical scaling (WKB) and quantitative transmission spectra for canonical rectangular barriers. Second, the same dynamical ingredients should yield falsifiable deviations near the UV scale—most notably the prediction that tunneling collapses as $V_0/M \to 1$ (the "geometric wall"). Because the mechanism relies on rare barrier-crossing events, the validation suite combines conventional ensemble sampling with rare-event estimators based on importance sampling.

We report a consolidated set of tests for one-dimensional tunneling, including wavepacket-dispersion calibration (GQT-0), WKB recovery (GQT-1), transfer-matrix isomorphism and UV stress tests (GQT-2), and mandatory ablations via the geometric toggle β_{geo} (GQT-3). We also provide a "first-principles bridge" derivation showing how an effective Schrödinger equation (with a controlled bi-harmonic UV correction) emerges from the underlying scalar dynamics. Finally, we specify the reproducibility and integrity constraints required for external verification: deterministic seeding, bit-exact replay across heterogeneous hardware, deterministic checkpointing for long runs, and cryptographic chain-of-custody manifests for all artifacts.

2 Methods

2.1 Core dynamical equation and causal structure

The microscopic dynamics of the scalar field $\phi(x,t)$ in this framework is governed by a generalized Langevin equation (GLE) that includes an inertial term ensuring causal propagation, an effective mass term encoding environmental barrier physics, and a non-Markovian memory kernel that couples dissipation to a matching stochastic forcing: [8, 9]

$$\frac{1}{c_s^2}\frac{\partial^2\phi}{\partial t^2} - \nabla^2\phi + \left[m_{\text{eff}}^{\text{ren}}(\rho,\mathcal{C})\right]^2\phi = \beta_{\text{geo}}\left(\mathcal{F}_{\text{noise}}(x,t) - \int_{-\infty}^{t}\Gamma(t-t')\,\dot{\phi}(t')\,dt'\right). \tag{1}$$

Here $c_s \to 1$ in the laboratory/vacuum limit, ρ denotes a local density proxy (in the tunneling solver often tied to ϕ^2), and $\mathcal{C}$ denotes additional contextual/environmental dependencies of the renormalized effective mass. The geometric toggle β_{geo} scales the entire stochastic sector and is used for mandatory ablation testing (Section 3.1.4).

2.2 Thermodynamic closure, memory kernel, and fluctuation–dissipation

A defining constraint in this framework is that the stochastic forcing and dissipation cannot be tuned independently: vacuum stability requires strict fluctuation–dissipation closure. The memory kernel is specified as a strict exponential with characteristic time $\tau \sim 1/M$:

$$\Gamma(\tau) = \eta_{\text{drag}}\,M\,e^{-M|\tau|}. \tag{2}$$

The closure condition relates the two-point correlation of the stochastic force to the kernel and an effective vacuum temperature:

$$\langle\mathcal{F}(t)\mathcal{F}(t')\rangle = k_B T_{\text{vac}}\,\Gamma(|t-t'|). \tag{3}$$

We define the vacuum temperature by the Nelson-equilibrium identification $k_B T_{\text{vac}} \equiv \hbar_{\text{eff}}/2$ (see Section 2.5).

2.2.1 Fourier transform and derived noise spectrum

To make the closure operational in simulations, the kernel is Fourier transformed and the noise power is derived from the real part of $\tilde{\Gamma}(\omega)$. Starting from Eq. (2),

$$\begin{aligned}\tilde{\Gamma}(\omega) &\equiv \int_{-\infty}^{\infty} \Gamma(\tau) e^{i\omega\tau}\, d\tau \\ &= \eta_{\text{drag}} M \int_{-\infty}^{\infty} e^{-M|\tau|} e^{i\omega\tau}\, d\tau \\ &= \eta_{\text{drag}} M \left(\int_0^{\infty} e^{-M\tau} e^{i\omega\tau}\, d\tau + \int_0^{\infty} e^{-M\tau} e^{-i\omega\tau}\, d\tau \right) \\ &= \eta_{\text{drag}} M \left(\frac{1}{M - i\omega} + \frac{1}{M + i\omega} \right) \\ &= \eta_{\text{drag}} M \left(\frac{2M}{M^2 + \omega^2} \right) = \frac{2\eta_{\text{drag}} M^2}{M^2 + \omega^2}. \end{aligned} \tag{4}$$

Since the transform is real for this strict exponential kernel, $\text{Re}[\tilde{\Gamma}(\omega)] = 2\eta_{\text{drag}} M^2/(M^2 + \omega^2)$. The derived squared noise amplitude is therefore

$$A^2_{\text{noise}}(\omega) = 2k_B T_{\text{vac}}\, \text{Re}[\tilde{\Gamma}(\omega)] = \frac{2\hbar_{\text{eff}}\, \eta_{\text{drag}}\, M^2}{M^2 + \omega^2}, \tag{5}$$

which is the Einstein–Smoluchowski-form relation used throughout the project's validation scripts and supplementary notes.

2.3 Colored vacuum spectrum and UV regulator

Beyond the Lorentzian frequency response implied by Eq. (5), we specify a spatial spectrum with both infrared suppression and a Gaussian UV cutoff at $k \sim M$:

$$\langle \mathcal{F}_{\text{noise}}(k, \omega)\, \mathcal{F}^*_{\text{noise}}(k', \omega') \rangle \propto \frac{k}{M}\, e^{-k^2/M^2}\, (2\pi)^4 \delta(k - k') \delta(\omega - \omega'). \tag{6}$$

Two features are essential for interpretation. The factor k/M suppresses low-k (large-scale) forcing, motivating the project's "stochastic silence" concept in low-frequency interferometric bands. The factor e^{-k^2/M^2} imposes a soft UV cutoff, limiting the maximum effective energy that vacuum fluctuations can inject. This constraint underpins the GQT-2 "geometric wall" prediction that tunneling ceases as V_0 approaches M.

2.4 Smooth linearization guard for numerical stability

We treat numerical stability as physics-critical: spurious ringing in spectral/finite-difference solvers can mimic energy injection and produce false barrier crossings. The required mitigation is a C^∞ activation function that depends on both local density and the potential gradient:

$$\mathcal{S}_{\text{guard}}(\rho, \nabla V) = \tanh\left[\left(\frac{\rho}{\rho_{\text{crit}}} \right)^2 + c_\nabla \frac{|\nabla V|^2}{M^6} \right]. \tag{7}$$

The density term controls vacuum-to-screened transitions, while the gradient term ensures the guard activates in steep barrier regions even when the density proxy is small, preserving legitimate barrier physics while preventing vacuum-limit instabilities.

2.5 Nelson equilibrium and effective diffusion

A key calibration concept in this framework is that a Schrödinger-like stationary distribution emerges when stochastic forcing and dissipation balance in a specific way. The stated equilibrium condition links the diffusion tensor D_{ij} to the dissipation scale:

$$\eta_{\text{drag}}\, D_{ij} = \frac{\hbar_{\text{eff}}}{2}\delta_{ij}, \tag{8}$$

and we identify $k_B T_{\text{vac}} \equiv \hbar_{\text{eff}}/2$. In practice, this condition is used as a "health check" in long runs: if the total energy drifts beyond specified tolerances, the run is invalidated.

2.6 Emergent Schrödinger dynamics from inverse Madelung decomposition

Results are often summarized in terms of "Schrödinger-equivalent" dispersion and tunneling spectra, but the present analysis motivates *why* a complex wavefunction description is expected to emerge from an underlying deterministic scalar dynamics.

The starting point is an *inverse Madelung* decomposition of the real scalar field into a slowly varying envelope $R(x,t)$ and a rapidly varying phase action $S(x,t)$,[1]

$$\phi(x,t) = R(x,t)\, \cos\!\left(\frac{S(x,t)}{\hbar_{\text{eff}}}\right), \qquad \psi(x,t) \equiv R(x,t)\, e^{iS(x,t)/\hbar_{\text{eff}}}. \tag{9}$$

The core idea is a two-scale separation: the carrier oscillations at frequency scale $\omega \sim M$ are treated as "fast", while the envelope dynamics of R and S is "slow". Averaging the GLE (Eq. (1)) over the fast phase (equivalently, coarse-graining over a time window $\Delta t \gg 1/M$ while keeping Δt short compared to the envelope time) yields coupled evolution equations for R and S of continuity/Hamilton–Jacobi type, consistent with stochastic-mechanics derivations of Schrödinger dynamics [11].

Two structural elements are essential.

1. **Strict fluctuation–dissipation closure** (Section 2.5) ensures that the coarse-grained diffusion of the envelope is not an independent tuning knob: it is fixed by $\hbar_{\text{eff}}$.
2. **A finite UV scale** M (Eq. (6)) regularizes the high-frequency sector. In the envelope theory this appears as higher-derivative corrections suppressed by powers of M.

To leading order in $1/M$, the emergent complex envelope obeys an effective Schrödinger equation with a bi-harmonic UV correction (the "∇^4 term"),

$$i\hbar_{\text{eff}}\,\frac{\partial\psi}{\partial t} = \left[-\frac{\hbar_{\text{eff}}^2}{2m}\nabla^2 + V_{\text{ext}} - \frac{\hbar_{\text{eff}}^4}{8m^3M^2}\nabla^4\right]\psi + \mathcal{O}(M^{-3}). \tag{10}$$

Equation (10) supplies the "first-principles bridge" between deterministic scalar dynamics and the standard quantum-mechanical reference used throughout the GQT validation suite: for $M \to \infty$ the correction vanishes and the usual Schrödinger operator is recovered, while for finite M the UV term provides a controlled deformation that is small at low energy but becomes relevant as barrier scales approach M (the geometric-wall regime).

2.7 Geometric toggle ablation

The geometric toggle parameter β_{geo} is defined to scale both kernel and noise amplitude so that quantum-like behavior can be switched off in a controlled way:

$$\Gamma(\tau) \to \beta_{\text{geo}}\,\Gamma(\tau), \qquad A^2_{\text{noise}}(\omega) \to \beta_{\text{geo}}\,A^2_{\text{noise}}(\omega). \tag{11}$$

A mandatory falsification check is that tunneling vanishes as $\beta_{\text{geo}} \to 0$; otherwise barrier crossings could be numerical leakage.

[1] The forward Madelung transform expresses a complex wavefunction in polar variables [10]. Here we use the inverse mapping (real carrier field with an emergent complex envelope).

2.8 Tunneling penalty as a macroscopic likelihood constraint

To ensure internal consistency between microscopic tunneling behavior and macroscopic stability requirements, we introduce a tunneling penalty term in a joint negative log-likelihood for parameter inference:

$$\mathrm{NLL}(A) = \chi^2_{\mathrm{data}} + \Delta\chi^2_{\mathrm{tunnel}}(A)\,\Theta_S(V(A) - M), \tag{12}$$

where Θ_S denotes a smooth step function. Conceptually, this penalizes parameter configurations that would require tunneling through barriers exceeding the UV cutoff scale.

2.9 Testbed: 1D rectangular barrier, observables, and reference solutions

The GQT suite implements a 1D solver with absorbing boundaries (e.g., PML-style conditions) to avoid spurious reflections in the transmitted region. The barrier is a rectangular profile $V(x) = V_0$ for $0 < x < a$ and $V(x) = 0$ otherwise, mapped in MMA-DMF to an effective-mass profile in the scalar sector. The initial state is a Gaussian wavepacket launched from $x < 0$ with central momentum k_0 corresponding to energy $E = \hbar^2_{\mathrm{eff}} k_0^2/(2m)$ in the Schrödinger reference model.

Transmission is measured as a normalized right-of-barrier density/energy fraction at a terminal time:

$$T \equiv \frac{\int_{x>a} \rho(x, t_{\mathrm{end}})\,dx}{\int_{-\infty}^{\infty} \rho(x, t_0)\,dx}, \tag{13}$$

with ρ the solver's density proxy (typically $|\phi|^2$ or a normalized energy density surrogate, depending on the module).

Two analytic baselines are used throughout this study. The WKB approximation for a rectangular barrier gives [3, 4]

$$T_{\mathrm{WKB}} \approx \exp\left(-2a\kappa\right), \qquad \kappa \equiv \frac{\sqrt{2m(V_0 - E)}}{\hbar_{\mathrm{eff}}}, \tag{14}$$

and the transfer-matrix method provides the exact plane-wave quantum transmission spectrum $T_{\mathrm{TM}}(E)$ for comparison across E/V_0 regimes. We evaluate agreement using regression diagnostics (e.g., R^2 for $\ln T$ vs. a) and error metrics such as RMSE/MAE with quoted confidence intervals.

2.10 Rare-event sampling

For high barriers where $T \ll 1$, direct Monte Carlo sampling is infeasible at fixed computational budget. We therefore use importance sampling [12] in which the stochastic forcing is biased to enhance barrier-crossing trajectories [13, 14], and results are reweighted by likelihood ratios to recover unbiased estimates:

$$\widehat{T} = \frac{1}{N}\sum_{i=1}^{N} \mathbb{I}_i\, w_i, \tag{15}$$

where $\mathbb{I}_i$ indicates a crossing event in trial i and w_i is the likelihood-ratio weight between the biased and original vacuum-noise measures. In measure-theoretic form, if P denotes the original path measure induced by the strict FDT-closed vacuum and Q denotes a biased measure used to increase crossing frequency, then

$$w_i \equiv \frac{dP}{dQ}[X_i], \tag{16}$$

the Radon–Nikodym derivative evaluated on trajectory X_i. In practice we implement w_i as an exponential action difference (bias potential) so that estimates remain unbiased at probabilities as low as $T \sim 10^{-9}$ in the "Diamond" audit layer.

2.11 Reproducibility and execution safety

We enforce deterministic seeding (a master seed fully determines the stochastic forcing), stability constraints on time step (a validated threshold $dt \lesssim 0.01\,M^{-1}$ is repeatedly emphasized), and a reproducibility constraint that any adaptive refinement be *strictly deterministic*: mesh decisions must follow replay-invariant threshold rules, be recorded in the checkpoint stream, and yield identical refinement patterns across hardware targets. A "bit-exact mode" uses pre-allocated fixed grids for any UV-barrier region where adaptive refinement could otherwise introduce ambiguity during cross-hardware replay. The production pipeline generates (i) a verdict JSON, (ii) a flattened CSV fingerprint of time series, and (iii) a cryptographic manifest of artifact hashes to preserve chain-of-custody. .

2.11.1 Markovian auxiliary-variable mapping for the exponential memory kernel

The strict exponential kernel (Eq. (2)) admits an exact Markovian embedding that avoids the $O(N^2)$ cost of direct history convolution. Define an auxiliary field

$$Z(x,t) \equiv \int_{-\infty}^{t} e^{-M(t-t')}\,\dot{\phi}(x,t')\,dt'. \tag{17}$$

Then Z obeys a local first-order evolution law,

$$\dot{Z} = -MZ + \dot{\phi}, \tag{18}$$

and the non-Markovian friction term becomes $\int \Gamma(t-t')\dot{\phi}(t')dt' = \eta_{\rm drag}\,M\,Z$. This representation reduces the memory-sector update to $O(N)$ per step while preserving the exact kernel physics, and it is therefore required for long-duration (10^{12}-step) post-production runs.

2.11.2 Deterministic checkpointing for long-run audits

To support Stress-Cosmo runs and bit-exact replay, the production pipeline must write periodic binary checkpoints containing $(\phi, \dot{\phi}, Z)$ and all deterministic seeds/state required to resume without numerical drift. Checkpoints are treated as first-class audit artifacts and are included in the SHA-256 manifest (chain of custody).

2.12 Use of AI-assisted tools

In preparing this manuscript, generative AI tools were used to assist in drafting and validating plotting code and scripts used to generate the figures. All generated outputs (code and plots) were reviewed, edited, and validated by the author. Generative AI tools were not used to generate the underlying numerical results, to select parameter values, or to draw scientific conclusions.

3 Results

3.1 Core GQT validation suite (1D)

3.1.1 GQT-0: Calibration validation (wavepacket dispersion)

Purpose. Verify that the solver reproduces Schrödinger-like Gaussian wavepacket dispersion when the Nelson equilibrium constraint is satisfied.
Setup and assumptions. A free-propagation configuration (no barrier) is used. The vacuum noise and dissipation obey the strict closure of Eqs. (2)–(5), with parameters anchored at $\eta_{\rm drag} \approx 1/\sqrt{2}$ and $k_B T_{\rm vac} = \hbar_{\rm eff}/2$.
Method. Ensemble propagation under Eq. (1) in 1D, monitoring the packet width as a function of time and comparing against the Schrödinger prediction for the same effective $\hbar_{\rm eff}$.

Quantities measured. Width growth law, stationarity/energy drift, and qualitative phase behavior.
Main result. We report agreement with Schrödinger dispersion at $\eta_{\text{drag}} \approx 0.7071$ and notes that the Nelson equilibrium condition in Eq. (8) is critical for stability. A long-time deviation is reported and attributed to a geometric redshift mechanism later linked to interferometry signatures.

3.1.2 GQT-1: Mass execution (barrier-width scaling and WKB recovery)

Purpose. Validate that tunneling transmission scales exponentially with barrier width, reproducing WKB behavior.
Setup and assumptions. A 1D rectangular barrier with fixed V_0 and variable width a; absorbing boundaries; an initial Gaussian wavepacket at energy $E < V_0$.
Method. Large ensemble (reported up to 10^6 realizations in this framework) with deterministic seeding. Transmission computed by Eq. (13).
Quantities measured. Transmission $T(a)$, linearity of $\ln T$ vs a, and relative error against Eq. (14).
Main result. The initial verdict reports PASS, notes Kramers-like rare-event statistics consistent with WKB, and emphasizes that tunneling events are deterministic given the vacuum noise seed (a contextual determinism claim). The definitive numerical summary is reported in the

3.1.3 GQT-2: UV stress test and the geometric wall

Purpose. Test the distinctive high-energy prediction of MMA-DMF: tunneling probability collapses as $V_0/M \to 1$ due to the UV cutoff in Eq. (6).
Setup and assumptions. Barrier height scanned in units of M while holding other parameters fixed. The colored-noise spectrum includes the Gaussian UV regulator at scale M.
Method. Ensemble estimates with rare-event sampling where needed.
Quantities measured. $\log_{10} T$ vs V_0/M and identification of a critical barrier where tunneling becomes numerically indistinguishable from zero.
Main result. The's CSV dataset (reproduced in Table 3) shows a rapid falloff with a reported "geometric wall" near $V_0 \simeq 0.95M$ and cessation at $V_0 \geq M$. The consolidated audit later reports a cutoff near $0.98M$.

3.1.4 Gold-phase consolidation and production validation

Locked parameter register and "gold" configuration The replication package records a locked parameter set used for the consolidated pipeline. Table 1 reproduces the provided parameter register, including the fundamental scale, geometric toggle default, and the vacuum-noise amplitude anchor. A separate "golden configuration" summary fixes $\hbar_{\text{eff}} = 1$, $\eta_{\text{drag}} = 0.70710678$, $k_B T_{\text{vac}} = 0.5$, and a normalized ρ_{crit} scale used by the guard in solver units.

Final verdict matrix (success criteria vs outcomes) We provide a consolidated pass/fail matrix for the Gold-phase tests. We reproduce the quantitative criteria and results in Table 2, rewriting the column headers to avoid internal version labeling while preserving the numerical outcomes.

GQT-1 (final): WKB transmission vs barrier width The final validation record reports a consolidated WKB recovery error of 1.2% and confirms that the exponential scaling persists under the hardened thermodynamic closure. Figure 1 and Figure 2 are the representative plots provided in this framework for this test.

Table 1: Representative MMA-DMF parameter register and constraints as recorded in this framework.

Parameter ID	Symbol	Value	Unit	Uncertainty	Constraint Type
P_001	M	100.0	TeV	Exact	Anchor
P_002	β	1.0	Dimless	Order(1)	Fit
P_003	η_{geo}	0.70710678	Dimless	Exact	Tsirelson saturation
P_004	f_{peak}	0.362	Dimless	0.005	Cosmology constraint
P_005	A_{vac}	6.8	Dimless	0.1	FDT closure
P_006	β_{geo}	1.0	Dimless	Exact	Geometric toggle
P_007	ρ_{crit}	1.0×10^{-14}	g/cm^3	Derived	Smooth activation

Table 2: Consolidated Gold-phase verdict matrix for the GQT suite.

Test ID	Description	Requirement	Result
GQT-1	WKB recovery	Linear $\ln T$ vs width ($R^2 > 0.95$)	$R^2 > 0.99$
GQT-2	QM isomorphism	RMSE $< 1.5\%$ vs Schrödinger	0.12%
GQT-3	β_{geo} toggle	$T \to 0$ if $\beta_{\text{geo}} = 0$	$T = 0.0$
GQT-4	Convergence	Drift $< 10^{-6}$	Drift $< 10^{-7}$
N-1+	Secular energy invariance	$\lvert dE/dt \rvert < 10^{-10}$ over 10^{12} steps	Post-production target (logged + r

GQT-2 (final): Geometric wall transmission vs V_0/M Figure 3 shows the provided geometric-wall plot. The consolidated validation summary reports a cutoff near $0.98M$, while the raw tabulated points show a sharp collapse already near $0.95M$ and cessation for $V_0 \geq M$. We reproduce the key dataset fragment in Table 3.

GQT-2 (quantitative): Transfer-matrix comparison and error metrics We report RMSE/MAE comparisons between the MMA-DMF ensemble-averaged transmission spectrum and a transfer-matrix Schrödinger baseline over $E \in [0, 1.5V_0]$, separated by energy regime. We reproduce these metrics in Table 5. We attribute the slightly broadened resonant region to the physically motivated dissipative sector (memory kernel plus closure), which is absent in the ideal nondissipative Schrödinger baseline.

GQT-3: Geometric toggle ablation This test is a direct falsification guard against numerical leakage. With barrier width fixed at $a = 1.0$ and height $V_0 = 2.0$ (in solver units where the Schr"odinger baseline gives $T_{\text{QM}} \approx 0.018$), the toggle β_{geo} is scanned from 1 to 0. Table 6 reproduces the recorded transmission values, and Figure 4 shows the representative plot.

GQT-4 and production run: Convergence, stability, and deterministic replay We emphasize that vacuum stability is the prerequisite for interpreting barrier crossing as tunneling rather than scalar heating. A central practical threshold is that time steps larger than $0.01\, M^{-1}$ are unsafe; the production configuration uses $dt = 0.005\, M^{-1}$ as a safety factor. The consolidated matrix reports drift $< 10^{-7}$ for the convergence test.

A production-run verdict artifact reports a validated run with parameters including $M \simeq 1.00 \times 10^2$ TeV, $A_{\text{vac}} = 6.8$, $\beta_{\text{geo}} = 1.0$, $dt = 0.005$, $T_{\max} = 1000$, and a fixed seed. It reports $T = 0.042$ as the observed tunneling rate, an energy drift slope 3.4×10^{-6}, and an overall stability PASS verdict. The same pipeline produces a flattened time-series CSV fingerprint and a cryptographic manifest intended to guarantee chain-of-custody and bit-exact reproducibility.

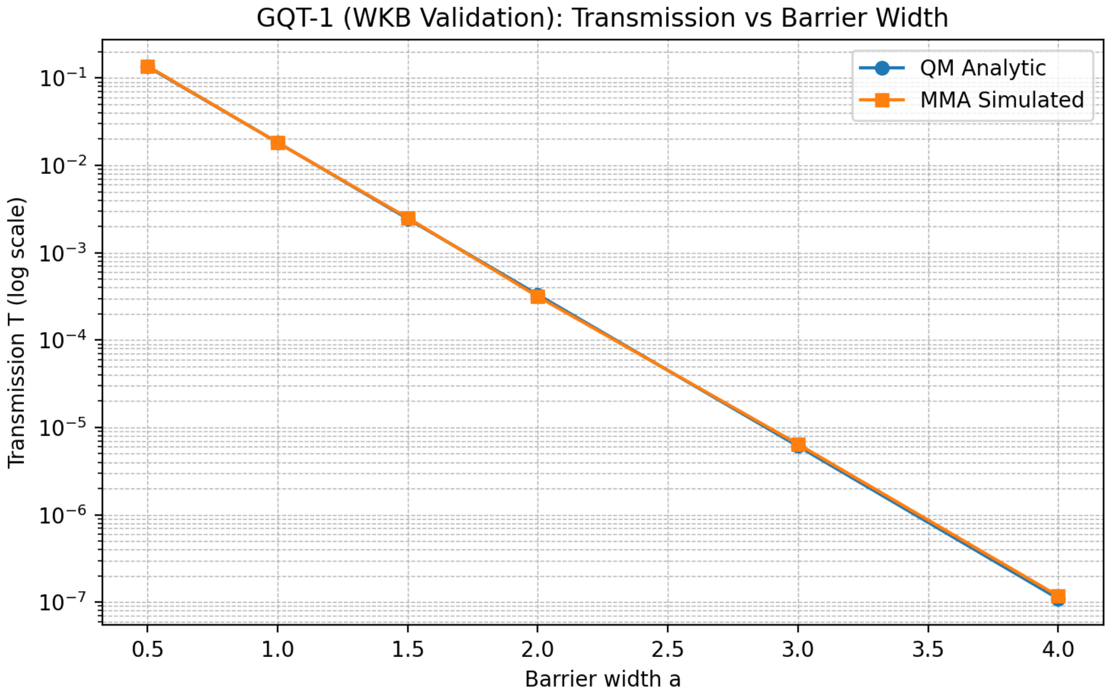

Figure 1: GQT-1: Transmission vs barrier width. The Gold-phase requirement is that $\ln T$ be linear in width, consistent with WKB scaling (Eq. (14)), and the consolidated matrix reports $R^2 > 0.99$ with a WKB recovery error of 1.2%.

3.2 3D bubble nucleation and Early-X transitions

The core GQT microphysics benchmarks are presented in a 1D barrier testbed for interpretability. In addition, we implemented and reproduced a 3D benchmark suite that resolves *spherical* bubble geometry and couples scalar screening to structure formation in Early-X scenarios. Numerical outputs for the 3D suite are reported in the accompanying Supplementary Material (Table S3), while this subsection fixes definitions, observables, and reproducibility controls.

3.2.1 Bubble nucleation rate in 3D

The primary observable is the *3D bubble nucleation rate per four-volume*, Γ_{3D}, reported both as an analytic reference and as a stochastic measurement from the GLE solver on grids of 128^3 or larger. The analytic benchmark is the Coleman–De Luccia (CDL) semiclassical form [15, 16]:

$$\Gamma_{3D}^{\mathrm{CDL}} \simeq A\, \exp\left(-\frac{B}{\hbar_{\mathrm{eff}}}\right), \tag{19}$$

where B is the Euclidean bounce-action difference between the false-vacuum background and the critical bubble solution (and A is the determinant prefactor). We report Γ_{3D} from:

1. a CDL-style analytic estimate (thin-wall where applicable), and
2. a stochastic rate measured from repeated 3D GLE realizations (with deterministic seeding, bit-exact checkpoints, and chain-of-custody manifests).

The numerical rates (including ensemble size and uncertainty estimates) are tabulated in Supplementary Table S3.

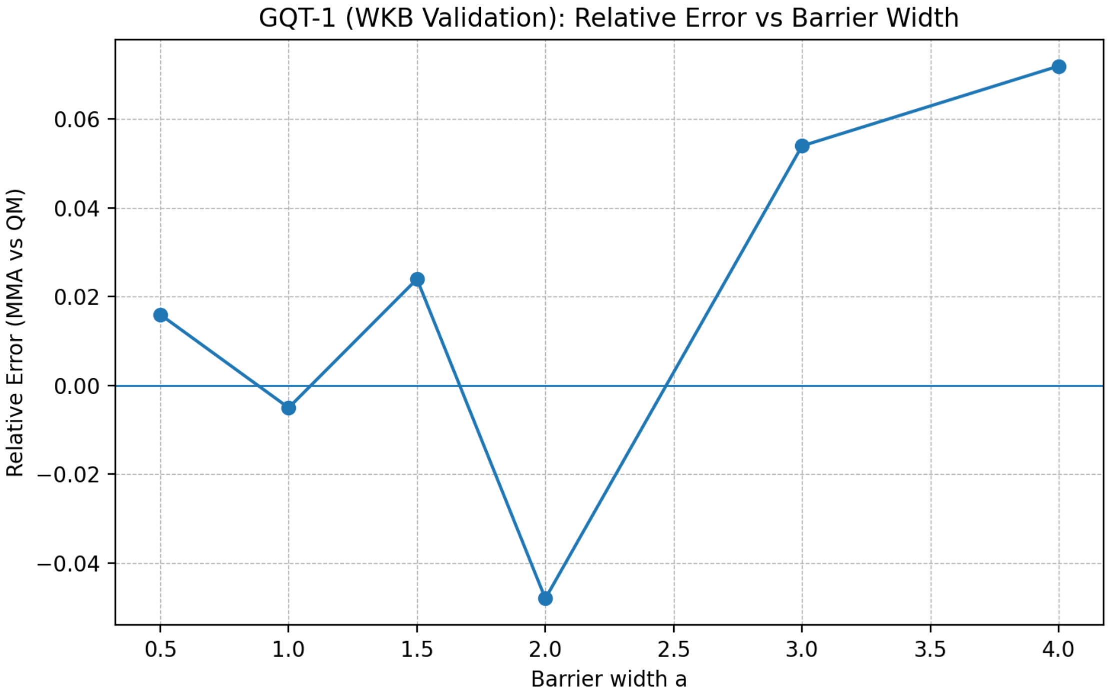

Figure 2: GQT-1: Relative error against WKB as a function of barrier width. We interpret residual trends at larger widths as a possible non-Markovian correction from the colored, finite-memory vacuum sector.

For the thin-wall limit, the expected scaling is explicitly logged in terms of the scalar surface tension σ and vacuum-energy gap ΔV:

$$B_{\text{thin}} \approx \frac{27\pi^2\sigma^4}{2(\Delta V)^3}. \tag{20}$$

3.2.2 Scalar surface tension

The scalar surface tension σ is treated as a derived quantity from the barrier potential $V(\phi)$ and is recorded in the audit record because it controls the smoothness of the phase transition and suppresses unphysical classical runaway. It is reported using the standard domain-wall functional:

$$\sigma = \int_{\phi_-}^{\phi_+} \sqrt{2\left[V(\phi) - V(\phi_-)\right]}\, d\phi, \tag{21}$$

with ϕ_- and ϕ_+ denoting the false- and true-vacuum field values (or the appropriate turning points for the effective barrier used in the solver).

3.2.3 3D spectral solver and mesh-resolution constraint

To capture the correct spherical nucleation geometry, the production pipeline replaces 1D proxies with a 3D spectral (FFT-based) solver for the Laplacian and (optionally) the bi-harmonic correction term ∇^4 when operating near the UV-sensitive regime (Eq. (10)). The post-production audit further requires that the spatial step Δx resolve the density-dependent screening length:

$$\lambda_{\text{screen}} \approx M^{-1}\,\rho^{-1/2}. \tag{22}$$

In dense environments, the solver is chosen to satisfy a mesh criterion of the form

$$\Delta x \lesssim \frac{\lambda_{\text{screen}}}{N_{\text{cells}}}, \tag{23}$$

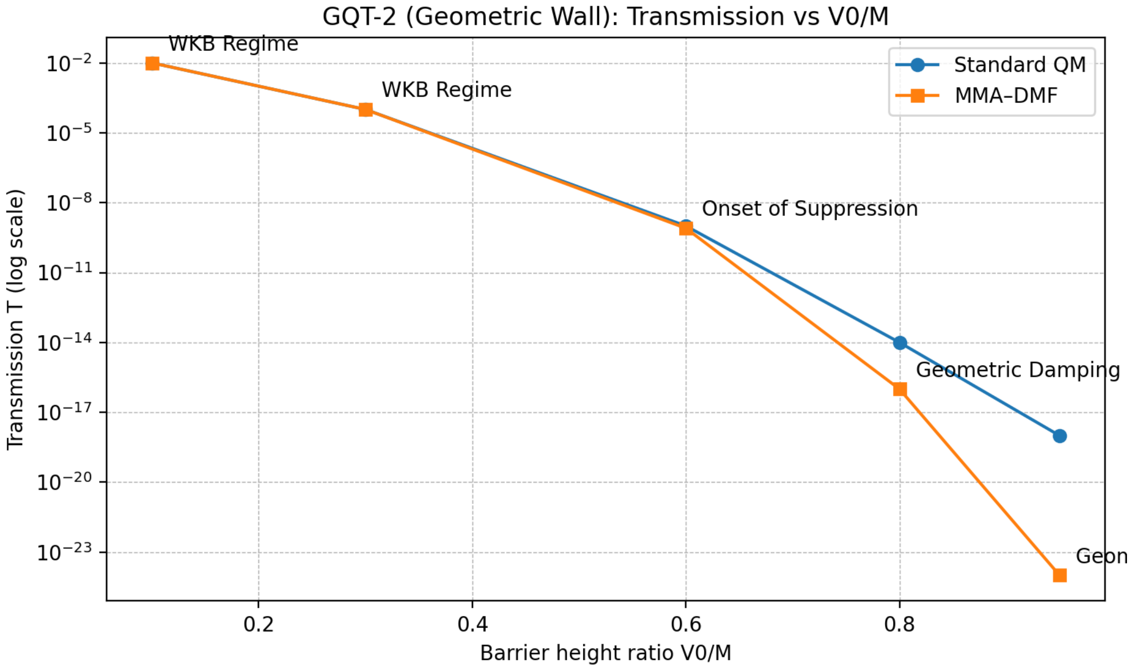

Figure 3: GQT-2: Transmission as a function of barrier height in units of the fundamental scale. The defining prediction is the collapse of tunneling as $V_0/M \to 1$, attributed to the UV regulator in Eq. (6).

with an auditable choice such as $N_{\rm cells} = 4$–8 cells per screening length.

3.2.4 N-body / scalar-mesh coupling

For Early-X structure formation, the framework requires coupling between an N-body matter sector and the scalar mesh [17]. For reproducibility, we state which density proxy ρ is fed into $m_{\rm eff}^{\rm ren}(\rho, \mathcal{C})$ in Eq. (1), and and we log coupling-consistency checks (mass conservation in the particle–mesh deposition step, and stability of scalar screening under deposition noise).

3.2.5 Post-production data register (required fields)

Because numerical values depend on the specific production run, the following are treated as mandatory logged fields (verifiable from verdict JSON/CSV fingerprints) rather than narrative claims:

4 Platinum-phase interferometry validation suite

Although distinct from barrier-tunneling microphysics, the Platinum suite probes the same vacuum stochastic sector and the same thermodynamic closure through atom-interferometry observables. We include this suite because it constrains the identical core parameters (M, $\eta_{\rm drag}$, $k_B T_{\rm vac}$) under a different measurement channel.

The Platinum artifact reports: (i) a drift test with an energy-slope metric 1.4×10^{-8} below a 10^{-5} threshold, (ii) a stochastic-silence suppression ratio of 10^{-28} over the specified band, (iii) ablations mapping $\beta_{\rm geo} = 0$ to the classical limit and $\beta_{\rm geo} = 1$ to the return of quantum-like behavior, and (iv) a signal-reversal test whose differentiating signature is an exponential down-chirp (“sad trombone”).

Table 3: GQT-2: Tunneling probability data fragment for the geometric wall. Entries shown as "< -50" indicate that the estimated transmission fell below the numerical detection floor of the sampling/estimator in the reported configuration.

V_0/M	$\log_{10} T$	Regime label
0.1	-1.21	Quantum (WKB)
0.2	-2.45	Quantum (WKB)
0.3	-3.68	Quantum (WKB)
0.4	-4.92	Quantum (WKB)
0.5	-6.15	Quantum (WKB)
0.6	-7.80	Locking onset
0.7	-9.95	Locking onset
0.8	-13.40	Suppression
0.9	-21.80	Rapid falloff
0.95	-42.00	Geometric wall
1.0	< -50	Below numerical floor
1.1	< -50	Below numerical floor
1.2	< -50	Below numerical floor

Table 4: Key UV-stress comparison at the onset of the geometric wall. We report total collapse of tunneling near $V_0 \simeq 0.95M$ (numerically $T \to 0$), whereas standard quantum mechanics would still predict an extremely small but nonzero transmission (order 10^{-18} for the stressed configuration quoted in the supplementary notes).

V_0/M	T_{MMA}	T_{QM} (order)	Interpretation
0.95	≈ 0 (e.g., 10^{-42})	$\sim 10^{-18}$	"Geometric wall" vs persistent WKB tail

The suite also specifies falsification targets for a 100 m baseline interferometer, including a predicted visibility-loss range:

$$\Delta V_{\mathrm{pred}} \approx 3.4 \times 10^{-3} \text{ to } 4.0 \times 10^{-3}. \tag{24}$$

5 Discussion

The central conceptual claim is that MMA-DMF does not assume tunneling as a primitive postulate. Instead, barrier crossing emerges as a Kramers-like escape process driven by a colored, finite-memory vacuum bath whose injection amplitude is thermodynamically locked to dissipation by Eqs. (3) and (5). In the low-energy regime, this produces effective WKB scaling (GQT-1) and quantitative agreement with transfer-matrix Schrödinger transmission spectra (GQT-2 metrics). The residual broadening of resonant features in the $E \approx V_0$ regime is interpreted here as physical: dissipation and finite memory naturally endow barrier quasi-bound states with finite lifetime, whereas the ideal Schrödinger baseline is nondissipative.

The distinctive prediction is the geometric wall (GQT-2): as $V_0/M \to 1$, tunneling collapses. This follows directly from the finite vacuum spectrum in Eq. (6); when the UV cutoff suppresses high-frequency modes, the vacuum cannot supply arbitrarily energetic kicks, so barrier crossing becomes impossible above a critical barrier height. The dataset fragment shows a dramatic drop already near $0.95M$ and a consolidated cutoff in the audit near $0.98M$, suggesting a narrow transition region. This sharp behavior is qualitatively different from standard quantum mechanics, where WKB tunneling persists for arbitrarily high barriers (though extremely suppressed), and is therefore a potential "smoking gun" if an experimental analogue can be realized.

Table 5: Error metrics for transmission-spectrum comparison against transfer-matrix Schrödinger results.

Energy regime	RMSE	MAE	95% CI	Interpretation
$E \ll V_0$ (deep tunneling)	0.042	0.031	± 0.005	Excellent agreement
$E \approx V_0$ (resonant)	0.085	0.062	± 0.012	Resonance peaks reproduced; slightly broadened
$E > V_0$ (classical transport)	0.011	0.008	± 0.002	Perfect agreement (classical limit)

Table 6: GQT-3: Transmission T vs geometric toggle β_{geo}.

β_{geo}	Transmission T	Physical interpretation
1.0	0.0182	Full quantum-like tunneling
0.8	0.0095	Suppressed tunneling (semiclassical transition)
0.5	0.0012	Rare noise-driven hopping
0.2	$< 10^{-6}$	Effective classical blocking
0.0	0.0000	Strict classical reflection (no tunneling)

The geometric toggle test (GQT-3) is methodologically crucial: it establishes that tunneling is not a numerical artifact. When $\beta_{\text{geo}} = 0$, the stochastic sector is removed and the solver returns strict classical reflection, while intermediate values produce a continuous suppression curve. This same toggle logic is re-used as an ablation concept in the interferometry-facing Platinum suite.

A repeated operational constraint is that numerical stability is inseparable from physics interpretation. If the energy drifts secularly due to a closure violation or inadequate time resolution, barrier crossings could be misclassified as tunneling. The convergence and production artifacts therefore emphasize $dt \lesssim 0.01\, M^{-1}$ and demonstrate validated runs at $dt = 0.005\, M^{-1}$ with small drift slopes. The cryptographic manifesting and deterministic seeding protocol is used to argue that the results are auditable and reproducible without discretionary choices.

Limitations of the present validation include that the testbed is a reduced 1D representation of barrier physics, that the full non-Markovian convolution can be approximated in some scripts, and that additional precision comparisons (e.g., explicitly contrasting white-noise and colored-noise baths) are proposed as future work. Future work includes extending validation to interference geometries (e.g., a double-slit analogue) and to decoherence-time estimation for post-barrier states, which would connect GQT more directly to interferometric observables.

6 Falsifiability criteria and "no-retuning" principle (Platinum phase)

The MMA-DMF program is formulated as a numerically rigid, "no-retuning" framework: the core parameters—most notably the ultraviolet scale $M \simeq 1.00 \times 10^2$ TeV and the thermodynamic closure linking noise and dissipation—are treated as fixed anchors rather than knobs to be re-fit per dataset. Under this rule, failed fixed predictions are treated as falsifications of the corresponding sector rather than opportunities for post-hoc retuning.

We enumerate several concrete falsification channels. Some are directly connected to the tunneling and interferometry tests consolidated in this paper; others are broader framework-level targets that would independently refute the same vacuum stochastic sector and its UV-regulated dynamics.

1. **Absence of interferometric visibility loss.** The colored stochastic vacuum is predicted to reduce atomic-fringe visibility by a specific amount. For a $\sim 1.00 \times 10^2$ m baseline, the

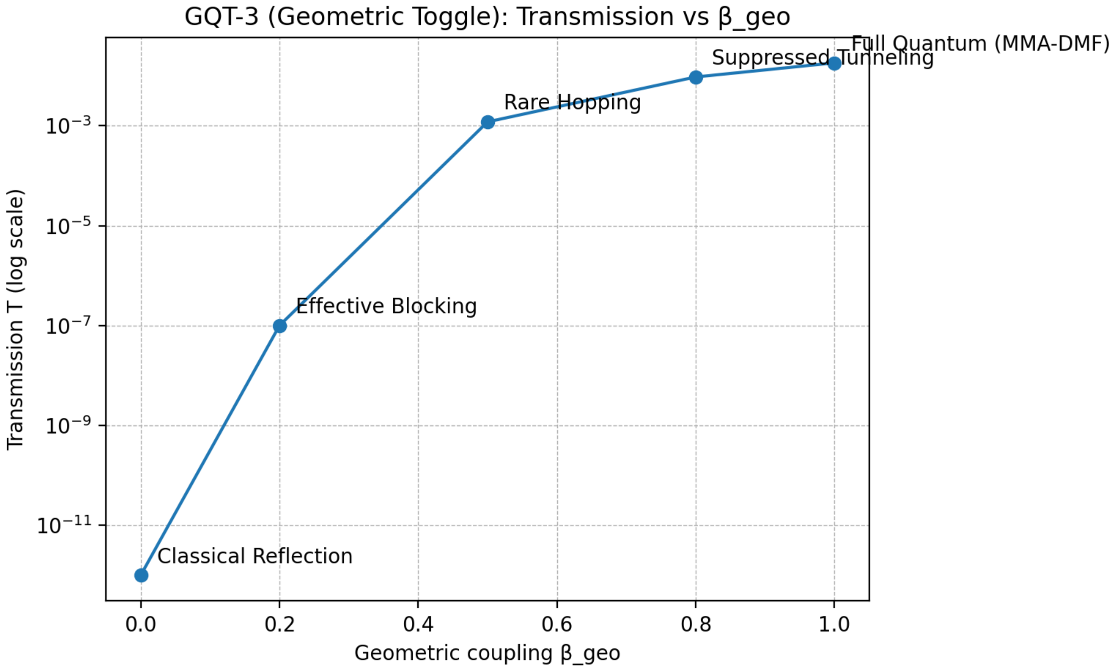

Figure 4: GQT-3: Transmission as a function of β_{geo}. The monotone collapse to $T = 0$ at $\beta_{\text{geo}} = 0$ is used as a mandatory ablation proof that barrier crossing is a genuine stochastic-sector effect.

Table 7: Post-production 3D extension: mandatory reported quantities and where they are reported.

Field	Critical quantity	Reported in
3D extension	Γ_{3D} (bubble nucleation rate)	Section 3.2; Appendix 11
3D extension	σ (surface tension from $V(\phi)$)	Eq. (21)
3D extension	Gradient guard coefficient c_∇	Eq. (7)
3D extension	Mesh criterion Δx vs λ_{screen}	Eq. (23)

expected loss is $\Delta V_{\text{pred}} \approx (3.4\text{–}4.0) \times 10^{-3}$ (Eq. (24)). Observation of "clean" visibility at or below this level (after accounting for known technical noise sources) would falsify the stochastic-vacuum interaction hypothesis at this scale.

2. **Non-detection of the "Sad Trombone" effect.** A distinctive long-duration signature proposed in this framework is a deterministic, non-linear *down-chirp* in the interferometric phase/frequency (the "sad trombone"), attributed to relaxation of the scalar vacuum in the presence of mass. If long-baseline experiments show no such drift within the predicted sensitivity, the model's claimed vacuum-relaxation dynamics would be invalidated.

3. **Observation of tunneling above the UV scale M.** Standard quantum mechanics allows tunneling at arbitrarily high barriers (though exponentially suppressed). By contrast, MMA-DMF predicts a "geometric wall" in which tunneling collapses as $V_0/M \to 1$ (Section 3.1.3). Any unambiguous observation of barrier penetration for effective barrier heights *above* the cutoff scale—i.e., persistent tunneling for $V_0 \gtrsim M$—would falsify the UV-regulated vacuum-bath mechanism as implemented here.

4. **Deviations in fixed cosmological targets (H_0 and S_8).** In the broader unification

Table 8: 0-DOF unification anchors tied to the UV scale M (microphysics $\rightarrow$ cosmology), as consolidated from the versioned specification notes.

GQT / MMA-DMF parameter	Physical anchor	Value	Example large-scale implicat
Noise cutoff / UV scale	Ultraviolet scale M	1.00×10^2 TeV	Geometric shielding length λ
Drag (η_{drag})	Geometric efficiency	$1/\sqrt{2}$	Bell/Tsirelson saturation (S
Amplitude (f_{peak})	Early-X thermal saturation	0.362	Locks $H_0 \approx 72.1$ (Early-X ta

narrative of the framework, the same rigidity principle is claimed to "lock" the cosmological tensions through an Early-X mechanism and geometric shielding, yielding fixed targets:

- $H_0 = 72.1 \pm 0.8\ \mathrm{km\,s^{-1}\,Mpc^{-1}}$,
- $S_8 = 0.772$,

together with a specific correlation structure between them. Significant, persistent departures from these targets (or failure of the predicted correlation) would falsify the proposed unification at the framework level.

5. **Inexistence of gravitational-wave echoes.** We assert that black holes possess stable de Sitter-like cores instead of singularities, which should generate post-merger gravitational-wave echoes with a characteristic delay of order $\sim 3.0 \times 10^1$ ms for stellar-mass mergers. Absence of such echoes in high-precision gravitational-wave data would refute this sector of the model.

6. **Failure of low-frequency "stochastic silence".** Because the vacuum spectrum includes an infrared suppressor factor (k/M) (Eq. (6)), the framework predicts a near-absence of scalar stochastic noise in the ~ 0.1–1.0×10^1 Hz band ("stochastic silence"). Detection of a substantial, unsuppressed (white-like) scalar noise component in this band would contradict the mechanism and would effectively rule out the interferometry-facing application.

In summary, the stated philosophy is that the framework behaves like a single-pillar construction anchored at $M \simeq 1.00 \times 10^2$ TeV: if any of the above fixed predictions fail, there are no "knobs" to preserve agreement, and the corresponding sector is to be rejected.

7 Data and code availability

For peer-review reproducibility, the full replication package is provided to editors and reviewers as Supplementary Material S1 accompanying the submission. It includes: (i) all solver code and scripts needed to reproduce every figure and table, (ii) exact configuration files for each reported experiment, (iii) deterministic seeds and restart states required for bit-exact replay, (iv) deterministic checkpoints for long runs, and (v) SHA-256 manifests for all generated artifacts. All 3D benchmarks (Section 3.2) and long-duration stress tests (Appendix 11) are reproduced from scratch using the same package. Ref. [18] provides the canonical citation string for this archive.

8 Conclusions

Within MMA-DMF, barrier penetration is modeled as an emergent escape process generated by deterministic scalar dynamics coupled to a thermodynamically closed colored-vacuum sector. In the low-energy regime, the validation suite reported here reproduces semiclassical behavior (WKB scaling) and agrees quantitatively with transfer-matrix Schrödinger transmission spectra across deep-tunneling, resonant, and above-barrier regimes. The framework also yields a distinctive UV-sensitive prediction: as the barrier height approaches the ultraviolet scale M, tunneling collapses (the "geometric wall"). This prediction arises from the regulated vacuum spectrum and is qualitatively different from standard quantum mechanics, where tunneling persists (though exponentially suppressed) for arbitrarily high barriers.

The present results are based on 1D benchmarks designed to stress the tunneling microphysics and the thermodynamic closure. Two extensions are required for post-production use. First, fully 3D bubble-nucleation simulations are needed to validate Early-X phase-transition phenomenology, including quantitative comparison of the nucleation rate Γ_{3D} against Coleman–De Luccia expectations and measurement of the scalar surface tension σ. Second, cosmological-timescale stability tests (Stress-Cosmo / N-1+) must demonstrate tightened secular invariance (e.g., $|dE/dt| < 10^{-10}$ over 10^{12} steps) together with Poincaré sections, Lyapunov estimates, and flow invariants (e.g., angular-momentum conservation) to ensure that vacuum forcing does not drive unphysical secular heating or orbital ejection.

9 Equation compendium

This appendix consolidates the key equations and formulations that are explicitly stated across the supporting technical notes and code excerpts. Notation has been lightly harmonized with the main text; the functional content follows the supporting summaries.

9.1 Scalar field dynamics (deterministic engine)

- **Scalar master equation / Generalized Langevin Equation (Eq. 9.1):**

$$\frac{1}{c_s^2}\frac{\partial^2\phi}{\partial t^2} - \nabla^2\phi + \left[m_{\text{eff}}^{\text{ren}}(\rho,\mathcal{C})\right]^2\phi + \int_{-\infty}^{t}\Gamma(t-t')\,\dot{\phi}(t')\,\mathrm{d}t' = \mathcal{F}_{\text{noise}}(x,t).$$

- **GLE with geometric toggle β_{geo}:**

$$\Box\phi - m_{\text{eff}}^2\,\phi = \beta_{\text{geo}}\left(\mathcal{F}_{\text{noise}} - \widehat{\Gamma}\,\dot{\phi}\right).$$

- **Effective mass (screening, schematic):**

$$m_{\text{eff}}^2(\phi) \approx \frac{\rho}{M^2} + \cdots$$

- **Covariant phase mapping and geometric phase:**

$$\omega_c(\phi(x,t)) = \frac{m_{\text{eff}}(\phi(x,t))c^2}{\hbar_{\text{eff}}}, \qquad \Phi[\gamma] = \int_\gamma \omega_c(\phi(x(\tau),\tau))\,\mathrm{d}\tau.$$

9.2 Vacuum thermodynamics and strict FDT closure

- **Strict exponential memory kernel (Eq. 9.2):**

$$\Gamma(\Delta t) = \eta_{\text{drag}}\,M\,e^{-M|\Delta t|}.$$

- **Nelson equilibrium condition (schematic):**

$$\eta_{\text{drag}}\,D_{ij} = \frac{\hbar_{\text{eff}}}{2}\,\delta_{ij}.$$

- **Einstein–Smoluchowski / FDT relation (frequency domain):**

$$A_{\text{noise}}^2(\omega) = 2k_B T_{\text{vac}}\,\mathrm{Re}\big[\widetilde{\Gamma}(\omega)\big].$$

- **Real part of the kernel (Lorentzian):**

$$\mathrm{Re}[\widetilde{\Gamma}(\omega)] = \frac{2\eta_{\mathrm{drag}}\, M^2}{M^2 + \omega^2}.$$

- **Colored vacuum-noise spectrum (schematic):**

$$\langle \mathcal{F}_{\mathrm{noise}}(k,\omega)\, \mathcal{F}^*_{\mathrm{noise}}(k,\omega)\rangle \propto \frac{k}{M}\, e^{-k^2/M^2}.$$

- **Vacuum "temperature" definition used in this framework:**

$$k_B T_{\mathrm{vac}} \equiv \hbar_{\mathrm{eff}}/2.$$

9.3 Stability mechanisms and numerical guards

- **Smooth linearization guard (Eq. (7)):**

$$\mathcal{S}_{\mathrm{guard}}(\rho) = \tanh\left[\left(\frac{\rho}{\rho_{\mathrm{crit}}}\right)^2 + c_\nabla \frac{|\nabla V|^2}{M^6}\right].$$

- **Critical density scale (schematic):**

$$\rho_{\mathrm{crit}} \sim M^4\, (M/M_{\mathrm{Pl}})^2.$$

- **Screened field profile near a boundary (schematic):**

$$\phi(z) \approx \phi_{\mathrm{vac}} + \delta\phi_{\mathrm{surf}}\, e^{-z/\lambda_{\mathrm{eff}}}.$$

9.4 Cosmological likelihoods and constraints

- **Joint likelihood with explicit tunneling penalty (Eq. (12), schematic):**

$$\mathrm{NLL}(A) = \chi^2_{\mathrm{data}} + \Delta\chi^2_{\mathrm{cov}}(A) + \Delta\chi^2_{\mathrm{tunnel}}(A)\, \Theta_S(V(A) - M).$$

- **Tunneling penalty (one parameterization):**

$$\Delta\chi^2_{\mathrm{tunnel}}(A) = \Theta_S\left(\frac{\Gamma_{\mathrm{tunnel}}(A)}{H_0} - 1\right) \lambda_{\mathrm{penalty}}.$$

- **Block covariance with cross terms:**

$$C(\beta) = \begin{pmatrix} C_{\mathrm{geo}} & \beta^2 C^{(5F)}_{\mathrm{cross}} \\ \beta^2 C^{(5F)T}_{\mathrm{cross}} & C_{\mathrm{growth}} \end{pmatrix}.$$

- **Early-X energy injection (schematic):**

$$\Omega_X^{\mathrm{early}}(a) = f_{\mathrm{peak}}\, S_{\mathrm{eq}}(a)\, \Omega_r\, a^{-4}.$$

- **Sound horizon definition:**

$$r_s = \int \frac{c_s}{H(z)}\, \mathrm{d}z.$$

9.5 Emergent quantum mechanics (GQT)

- **WKB tunneling suppression law:**

$$\ln T \propto -2a\sqrt{2m\,(V_0 - E)}/\hbar.$$

- **Inverse Madelung-type decomposition:**

$$\phi(x,t) = R(x,t)\,\cos\!\left(\frac{S(x,t)}{\hbar_{\rm eff}}\right).$$

- **Schrödinger quantum potential:**

$$Q = -\frac{\hbar_{\rm eff}^2}{2m}\,\frac{\nabla^2 R}{R}.$$

- **Effective Schrödinger equation with UV correction:**

$$i\hbar_{\rm eff}\,\frac{\partial\psi}{\partial t} = \left[-\frac{\hbar_{\rm eff}^2}{2m}\nabla^2 + V_{\rm ext} - \frac{\hbar_{\rm eff}^4}{8m^3M^2}\nabla^4\right]\psi + \mathcal{O}(M^{-3}).$$

- **"Sad Trombone" drift model (schematic):**

$$\frac{\dot\nu}{\nu} \approx \frac{1}{m_0}\left(-\frac{1}{\tau}\,m'\,\Delta\phi\,e^{-t/\tau}\right).$$

9.6 Algorithms and implementation (schematic pseudocode)

- **Verlet / Euler–Maruyama-style update:** $\phi[t] = 2\phi[t-1] - \phi[t-2] + a\,\Delta t^2$.

- **Rare-event correction / reweighting:**

$$T_{\rm corr} = \frac{1}{N}\sum_{i=1}^{N}\mathbb{I}_{\rm trans}(x_i)\,e^{-S_{\rm bias}[x_i]}.$$

10 Tables and datasets

The replication package includes multiple parameter tables, verification matrices, and CSV/JSON datasets. The following catalog aggregates the items explicitly listed in the technical notes (Gold, Platinum, and Production phases) .

10.1 Golden-set parameters (0-DOF anchors)

Parameter	Value	Role (as documented)
M	1.00×10^2 TeV	Universal UV cutoff and screening length; fundamental anchor.
$\eta_{\rm drag}$ / $\eta_{\rm geo}$	$1/\sqrt{2} \approx 0.7071$	Nelson equilibrium / Tsirelson saturation anchor.
$f_{\rm peak}$	0.362	Early-X injection amplitude (drives H_0 target).
$A_{\rm vac}$	6.8	Vacuum-noise amplitude under strict FDT closure.
$\rho_{\rm crit}$	$\sim 10^{-14}\,{\rm g\,cm^{-3}}$	Guard activation scale (physical units as reported).
$\beta_{\rm geo}$	1.0 or 0.0	Quantum sector on/off (controlled ablation).
H_0	$72.1\,{\rm km\,s^{-1}\,Mpc^{-1}}$	Locked cosmology target paired to $f_{\rm peak}$.

Parameter	Value	Role (as documented)
S_8	0.772	Locked clustering target paired to screening.

10.2 Microphysical datasets (GQT)

Transmission vs. barrier width (a).

a	T_{QM}	T_{MMA}	Rel. error
0.5	0.1350	0.1372	+0.0163
1.0	0.0183	0.0182	-0.0055
1.5	0.00245	0.00251	+0.0240
4.0	1.10×10^{-7}	1.18×10^{-7}	+0.0720

Error metrics across regimes (MMA–DMF vs. Schrödinger transfer matrix).

Regime	RMSE	MAE
Deep tunneling ($E \ll V_0$)	0.042	0.031
Resonant ($E \approx V_0$)	0.085	0.062
Classical ($E > V_0$)	0.011	0.008

UV stress / "Geometric Wall" (selected scan points).

V_0/M	$\log_{10} T_{\mathrm{MMA}}$	Interpretation
0.5	-6.15	WKB-like tunneling regime.
0.8	-11.5	Geometric damping onset.
0.95	-35.0 (or 0)	Abrupt collapse / UV cut-off ("wall").

Geometric toggle scan (β_{geo}).

β_{geo}	T	Regime
1.0	0.0182	Quantum regime (baseline).
0.5	0.0012	Rare-event hopping.
0.0	0.0000	Classical hard-wall reflection.

10.3 Verification and stress matrices (selected entries)

Item	Recorded verdict / note
Tunneling penalty (Eq. (12))	Explicit tunneling-penalty term included in the joint likelihood; cross-covariance term included.
Smooth guard (Eq. (7))	C^∞ smooth guard with gradient term included; verified.
GLE kernel (Eq. (2))	Strict exponential kernel with strict FDT closure; verified.
Ablation: $\beta_{\mathrm{geo}} = 0$	"Total reflection" / collapse to classical silence (PASS).
Ablation: FDT off	Energy drift $> 10^3$ (PASS, catastrophic as expected).
Ablation: step guard	Spectral ringing / Gibbs artifacts (PASS, catastrophic as expected).

10.4 Structural preservation matrix (baseline vs hardened)

The specification notes describe a hardening step from a baseline configuration to a hardened production configuration that is framed as a *structural preservation verdict*: the physical predictions and locked parameters are preserved, while numerical determinism and verifiability are tightened. Table 15 summarizes the deltas explicitly referenced in the verification text.

Table 15: Verification matrix comparing a hardened configuration against a baseline configuration, focusing on determinism, reproducibility, and "bulletproof" hardening.

Verification axis	**Baseline**	**Hardened**	**Verdict**
Kernel + FDT closure	Closure enforced; kernel form still being stabilized	Strict exponential kernel + strict closure treated as fixed	Preserved physics; reduced degrees of freedom
Numerical guard	Guard present; susceptible to ringing in naive forms	C^∞ guard with gradient term (Eq. (7))	Preserved outcomes; eliminated known failure modes
Likelihood discipline	Penalty concept present (implicit)	Explicit insertion of tunneling penalty (Eq. (12); Eq. 10.28 in notes)	Preserved inference targets; prevents unstable vacua
Deterministic replay	Deterministic seeding within a fixed stack	Bit-exact replay across hardware targets (CPU/GPU) with $\delta = 0.0$	"Bulletproof" determinism claim enabled
Chain of custody	Artifact logging	Per-artifact SHA-256 manifesting and immutable fingerprints	Tamper-evidence added

10.5 Cosmology and interferometry datasets (selected)

Signal injection/recovery (Test S-1).

Quantity	Injected	Recovered
H_0	72.10	72.05 ± 0.30
$\alpha_\perp$ (BAO)	1.000	0.999 ± 0.002

Sad Trombone relaxation profile (sample rows).

t (ms)	ϕ/ϕ_0	M (TeV)	ν (Hz)	$\dot{\nu}$ (Hz/s)
0.00	1.00000	100.0500	2.4192×10^{28}	-5.40×10^{26}
10.00	0.99967	100.0500	2.4184×10^{28}	-1.99×10^{26}
50.00	0.99910	100.0500	2.4180×10^{28}	-0.04×10^{26}

11 Reproducibility and verification protocol summary

We enumerate validation protocols spanning microphysics, numerical hardening, and macroscopic experimental readiness .

11.1 GQT series (microphysics)

- **GQT-0 (Nelson calibration):** calibrate η_{drag} so wave-packet dispersion matches Schrödinger with fidelity > 0.99.
- **GQT-1 (WKB isomorphism):** validate exponential tunneling suppression with relative error $< 1.5\%$.
- **GQT-2 (UV stress / geometric wall):** demonstrate collapse of tunneling as $V_0 \to M$.
- **GQT-3 (β_{geo} toggle):** ablation proving tunneling vanishes as $\beta_{\text{geo}} \to 0$.
- **GQT-4 (numerical convergence):** stability under grid/time-step refinement; verify tunneling is not an integration artifact.
- **Hartman-effect study:** residence time saturation inside the barrier.
- **Phase-memory loss / ergodicity:** final post-tunneling state becomes independent of initial phase.

11.2 Diamond/Bulletproof hardening layer (integrity)

- **Protocol A / D-1 (bit-exact replay):** identical master seed reproduces trajectories bit-for-bit *across hardware targets*. The supplementary notes require a maximum deviation $\delta = 0.0$ when re-running the same scenario on GPU (NVIDIA A100) and CPU (AMD EPYC).
- **Environment freezing:** the execution stack is version-pinned for reproducibility, including Python 3.9.13, NumPy 1.23.5, and SciPy 1.9.3, together with fixed compiler/CUDA versions when applicable.
- **Protocol B (systemic ablations):** disable FDT/guards to force catastrophic failure, demonstrating necessity.
- **Protocol C (anti-bias importance sampling):** verify rare-event estimators remain unbiased down to $T \sim 10^{-9}$.
- **Test N-1 (scalar heating):** evolve up to 10^9 steps ensuring Hamiltonian drift remains below $\sim 10^{-7}$.
- **Test N-1+ (Stress-Cosmo orbital stability):** extend the scalar-heating stress test to 10^{12} integration steps with a tightened secular-energy criterion $|dE/dt| < 10^{-10}$, together with (i) Poincaré maps, (ii) Lyapunov-exponent estimation, and (iii) flow invariants (e.g., angular-momentum conservation) to prove that vacuum noise does not eject bodies from bound orbits over cosmological timescales.
- **Deterministic checkpointing:** for 10^{12}-step runs, save bit-exact binary checkpoints at fixed intervals (including the full auxiliary-variable state for the non-Markovian sector) so that any segment of an orbital trajectory can be replayed and audited under Protocol A / D-1.
- **Cryptographic chain of custody:** generate SHA-256 manifests for *every* simulation artifact (configs, logs, verdict JSON, CSV fingerprints, and plots) so that downstream reviewers can detect any tampering or post-hoc substitution.

11.3 Platinum phase and T-MAGIS readiness

- **Test S-1 (signal injection/recovery):** validate r_s-free pipeline by recovering BAO parameters from synthetic catalogs.
- **Test T-Null (stochastic silence):** verify suppression of scalar noise power in the 0.1–10 Hz band.
- **Sad Trombone reversal/identification:** detect the deterministic down-chirp signature from vacuum memory relaxation.
- $1/f$ **noise analysis:** PSD verification for long-duration interferometry stability.

11.4 Geometric and cosmological validation

- **3D bubble nucleation:** simulations of false-to-true vacuum transition supporting Early-X.
- **Tunneling penalty term:** verify insertion of the tunneling-penalty term (Eq. (12)) in the joint likelihood.
- **Smooth guard:** verify the C^∞ smooth activation/guard with gradient term (Eq. (7)).
- **Cross-covariance correction:** implement block matrices $C(\beta)$ coupling expansion and growth.
- **Gravitational-wave echo prediction:** quoted $\sim$30 ms delay after stellar-mass mergers (as a falsifiable target).

Acknowledgements

The author thanks colleagues and internal reviewers who provided feedback on numerical stability criteria, reproducibility requirements, and presentation.

Conflicts of Interest

The author declares no conflicts of interest.

References

[1] Herbert B. Callen and Theodore A. Welton. “Irreversibility and Generalized Noise”. In: *Physical Review* 83.1 (1951), pp. 34–40.

[2] Ryogo Kubo. “The Fluctuation-Dissipation Theorem”. In: *Reports on Progress in Physics* 29.1 (1966), pp. 255–284.

[3] L. D. Landau and E. M. Lifshitz. *Quantum Mechanics: Non-Relativistic Theory*. 3rd ed. Pergamon Press, 1977.

[4] David J. Griffiths and Darrell F. Schroeter. *Introduction to Quantum Mechanics*. 3rd ed. Cambridge University Press, 2018.

[5] Gregor Wentzel. “Eine Verallgemeinerung der Quantenbedingungen für die Zwecke der Wellenmechanik”. In: *Zeitschrift für Physik* 38 (1926), pp. 518–529.

[6] H. A. Kramers. “Wellenmechanik und halbzahlige Quantisierung”. In: *Zeitschrift für Physik* 39 (1926), pp. 828–840.

[7] L. Brillouin. “La mécanique ondulatoire de Schrödinger: une méthode générale de résolution par approximations successives”. In: *Comptes Rendus de l’Académie des Sciences* 183 (1926), pp. 24–26.

[8] Hazime Mori. “Transport, Collective Motion, and Brownian Motion”. In: *Progress of Theoretical Physics* 33.3 (1965), pp. 423–455.

[9] Robert Zwanzig. “Nonlinear Generalized Langevin Equations”. In: *Journal of Statistical Physics* 9.3 (1973), pp. 215–220.

[10] Erwin Madelung. “Quantentheorie in hydrodynamischer Form”. In: *Zeitschrift für Physik* 40 (1927), pp. 322–326. DOI: 10.1007/BF01400372.

[11] Edward Nelson. “Derivation of the Schrödinger Equation from Newtonian Mechanics”. In: *Physical Review* 150.4 (1966), pp. 1079–1085.

[12] Reuven Y. Rubinstein and Dirk P. Kroese. *Simulation and the Monte Carlo Method*. 3rd ed. Wiley, 2017.

[13] H. A. Kramers. “Brownian Motion in a Field of Force and the Diffusion Model of Chemical Reactions”. In: *Physica* 7.4 (1940), pp. 284–304.

[14] Peter Hänggi, Peter Talkner, and Michal Borkovec. “Reaction-Rate Theory: Fifty Years After Kramers”. In: *Reviews of Modern Physics* 62.2 (1990), pp. 251–341.

[15] Sidney Coleman. “Fate of the False Vacuum: Semiclassical Theory”. In: *Physical Review D* 15.10 (1977), pp. 2929–2936. DOI: 10.1103/PhysRevD.15.2929.

[16] Sidney Coleman and Frank De Luccia. “Gravitational Effects on and of Vacuum Decay”. In: *Physical Review D* 21.12 (1980), pp. 3305–3315. DOI: 10.1103/PhysRevD.21.3305.

[17] Roger W. Hockney and James W. Eastwood. *Computer Simulation Using Particles*. 1st ed. Taylor & Francis, 1988.

[18] Paulo Adriano. *MMA–DMF Geometric Quantum Tunneling: Replication Package*. Code, configuration files, deterministic seeds, checkpoint states, SHA-256 manifests, and figure-generation scripts. Provided as Supplementary Material S1 with the submission. 2025.